Catalysis Science & Technology

ROYAL SOCIETY OF CHEMISTRY

PAPER

View Article Online
View Journal | View Issue

Cite this: *Catal. Sci. Technol.*, 2021, 11, 4581

Tuning the degradation activity and pathways of chlorinated organic pollutants over CeO_2 catalyst with acid sites: synergistic effect of Lewis and Brønsted acid sites†

Xuelong Lv,[ab] Songcai Cai,[ab] Jin Chen,[ab] Dongxu Yan,[ab] Mingzhu Jiang,[ab] Jing Chen [bc] and Hongpeng Jia *[ab]

Received 9th April 2021,
Accepted 17th May 2021

DOI: 10.1039/d1cy00626f

rsc.li/catalysis

Enhancing the surface acidity has been seen as an effective strategy to optimize the performance of catalysts for the degradation of chlorinated volatile organic compounds (CVOCs). Herein, a series of catalysts are constructed by introducing Lewis and Brønsted acid sites into the skeleton surface of three-dimensional ordered macroporous (3DOM) CeO_2. By a systematic study, we find that the introduction of Lewis acid sites can enhance the redox capacity of CeO_2, while the surface Brønsted acid sites of the material promote chlorobenzene (CB) degradation through hydrolysis that is an effective degradation route to generate less chlorinated organic by-products. The optimal S–$Ce_{0.7}Zr_{0.3}O_2$ with both abundant surface Lewis and Brønsted acid sites presents a stable activity and only 1.2% Cl_2 selectivity with ~90% CB conversion at 410 °C for 24 h. This work reveals the different roles and synergistic effects of Lewis and Brønsted acid sites to develop environmentally friendly CVOC combustion catalysts.

1. Introduction

Chlorinated volatile organic compounds (CVOCs) represented by chlorobenzene (CB) are considered as hazardous pollutants, which not only are important precursors of extremely toxic dioxins but also harm the ecological environment and human health.[1–3] Whether from the perspective of public safety or ecological protection, it is necessary to issue stricter emission regulations and develop an efficient CVOC removal technology. Among the numerous CVOC elimination technologies, catalytic oxidation is undoubtedly the most widely used and most promising strategy.[4] The core of this technique is the design and development of a suitable catalyst, which should be adapted to practical application scenarios. However, there are two key challenges that need to be overcome due to the unique C–Cl bond of CVOC molecules, in which one is about enhancing the chlorine tolerance of catalyst to promote their stability, and the other is to restrain the production of highly toxic by-products.[5–7]

In previous studies, the Deacon reaction (the oxidation of adsorbed Cl species to Cl_2, or $HCl + O_2 \rightleftharpoons H_2O + Cl_2$) was used to address the first challenge.[8–13] With the doping of transition metal cations or loading of Ru, the strength of surface Lewis acid (high valence metal ions and oxygen vacancy *etc.*) and Deacon reactivity of the base material are enhanced, which accelerates the fracture of the M–Cl bond and the desorption of inorganic chlorine species (ICs), thus improving the chlorine tolerance of the catalyst. According to the literature, the Ce–Ti catalytic system exhibits excellent durability for 1,2-dichloroethane (DCE) oxidation at low temperature.[14] The doping of Mn ions can significantly improve the catalytic activity and stability of CeO_2 materials on trichloroethylene (TCE) oxidation.[15] In addition, Ru/Ti_x-Sn_{1-x} catalysts have been reported for catalytic oxidation of dichloromethane (DCM) and CB.[8] The results of stability tests show that the introduction of Ru improves the stability of DCM oxidation greatly. Similar results have also been observed in other catalytic systems, such as Ru/TiO_2, Ru/Co_3O_4, Ru/Ce_xAl_y, Ru/CeO_2 *etc.*[6,10,16,17] However, it has to be mentioned that Cl_2, the representative product of the Deacon reaction, has an extremely high environmental risk and can cause a mass of polychlorinated organic by-products.

Recently, the important role of Brønsted acid in catalytic degradation of CVOCs has been repeatedly mentioned.[18–20] It

[a] *CAS Center for Excellence in Regional Atmospheric Environment, and Key Laboratory of Urban Pollutant Conversion, Institute of Urban Environment, Chinese Academy of Sciences, Xiamen, 361021, China. E-mail: hpjia@iue.ac.cn; Fax: +86 592 6190767; Tel: +86 592 6190767*
[b] *University of Chinese Academy of Sciences, Beijing, 100049, China*
[c] *Xiamen Institute of Rare-earth Materials, Haixi Institutes, Chinese Academy of Sciences, Xiamen, Fujian 361021, China*

† Electronic supplementary information (ESI) available. See DOI: 10.1039/d1cy00626f

has been confirmed that the Brønsted acid sites on the surface of a catalyst can facilitate the removal of Cl poisoning species in the form of HCl, thus resulting in stability enhancement.[21] The role of Brønsted acids can be well explained in the perspective of a reaction mechanism while a novel hydrolytic destruction route for efficient CVOC elimination is proposed.[22] Obviously, the introduction of Brønsted acid sites on the surface of a catalyst is a promising strategy to address both of the two aforementioned challenges. To ensure sufficient oxidation capacity and anti-coking capacity, Lewis acid sites should also be appropriately present on the surface of catalysts as redox active sites.[23,24] Therefore, in this work, a catalytic system based on the regulation of surface Lewis and Brønsted acids was constructed to achieve the efficient degradation of CB, a typical pollutant of CVOCs. In particular, Lewis acid was introduced into the substrate by doping with high valence state Zr ions, while the introduction of S, P, W, or Mo into CeO_2 can effectively enhance the surface Brønsted acids.[5,6,21,25] The materials were synthesized into a three-dimensional ordered macroporous (3DOM) structure to efficiently promote the high dispersion of acid sites on the material surface and the full contact between pollutant molecules and active sites.

2. Experimental section

2.1 Chemicals and reagents

All chemicals for the preparation of catalysts were A.R. grade without any further purification. $ZrOCl{\cdot}8H_2O$ (98.0%), methyl methacrylate (99.0%), and $K_2S_2O_8$ (99.5%) were purchased from Shanghai Macklin Biochemical Co., Ltd. (Shanghai, China). $Ce(NO_3)_3{\cdot}6H_2O$ (99.95%) was obtained from Shanghai Aladdin Bio-Chem Technology Co., Ltd. (Shanghai, China). Methanol (99.5%), $(NH_4)_2SO_4$ (99.0%), $(NH_4)_3PO_4{\cdot}3H_2O$ (95.0%), $H_{40}N_{10}O_{41}W_{12}{\cdot}xH_2O$ (90.0%), and $(NH_4)_6Mo_7O_{24}{\cdot}4H_2O$ (99.0%) were purchased from Sinopharm Chemical Reagent Co., Ltd. (Shanghai, China).

2.2 Catalyst preparation

$Ce_{1-x}Zr_xO_2$ (x = 0, 0.1, 0.3, 0.5, and 1, is the molar ratio of Zr/(Ce + Zr)) was synthesized *via* the colloidal crystal template (CCT) pathway, using polymethyl methacrylate (PMMA) arrays as a macroporous template. The well-arrayed PMMA microspheres were synthesized and assembled through an emulsifier-free emulsion polymerization method reported in previous literature.[26] In a typical process, a stoichiometric mole ratio of the precursors, cerium nitrate hexahydrate and dichlorooxozirconium were dissolved in 10 mL methyl alcohol to obtain a homogenous solution with a total metal molar concentration of 2 mol L^{-1}. Then, 2 g PMMA template was added to the solution and the mixture was allowed to stand undisturbed for 6 h. After complete impregnation of the PMMA microspheres, the excess precursor solution was removed by vacuum filter and the PMMA arrays were dried overnight in a vacuum oven at 50 °C. The above product was first calcined at 310 °C for 3 h with a ramp of 1 °C min^{-1} and then cooled to room temperature under a 100 mL min^{-1} nitrogen flow, and finally the atmosphere was changed to 100 mL min^{-1} air to calcine powders at 550 °C for 10 h with a ramp of 1 °C min^{-1}, thus obtaining the $Ce_{1-x}Zr_xO_2$ samples.

To introduce Brønsted acids on the skeleton surface of $Ce_{0.7}Zr_{0.3}O_2$, an incipient wetness method was used to synthesize M–$Ce_{0.7}Zr_{0.3}O_2$ (M = S, P, W, or Mo). In the process of modification, ammonium sulfate, ammonium orthophosphate, ammonium tungstate, and ammonium molybdate were used as precursor reagents to realize the modification of materials by different elements. After 4 h of impregnation, the samples were dried in a vacuum oven at 50 °C overnight and calcined at 550 °C in air for 3 h. For the obtained samples, the actual element load is about 1 wt%.

The used samples were obtained after a reaction cycle under experimental conditions: concentration of CB c(CB) = 1000 ppm, weight hourly space velocity (WHSV) = 60 000 mL g^{-1} h^{-1}, H_2O content = 0 vol%. The monolithic catalyst was prepared by vacuum coating, and a cylindrical cordierite honeycomb ceramic with 32 mm diameter and 50 mm height was chosen as the carrier. After loading S–$Ce_{0.7}Zr_{0.3}O_2$, the sample was calcined at 550 °C in air for 3 h. According to the weight change, the actual amount of S–$Ce_{0.7}Zr_{0.3}O_2$ load was approximately 1 g.

2.3 Catalyst characterization

In order to characterize the microstructure and surface properties of samples, a variety of characterization techniques were used. The crystal structure of the samples was observed by powder X-ray diffraction (XRD) measurement on a PANalytical X'pert Pro diffractometer equipped with an X-ray radioactive source of Cu-Kα at the 2θ angle range from 10° to 90°. Nitrogen adsorption and desorption isotherms were obtained at 77 K using a physisorption instrument from Quantachrome Autosorb IQ operated in static measurement mode. The specific surface area and pore size distribution of samples were calculated using the Brunauer–Emmett–Teller (BET) and Barrett–Joyner–Halenda (BJH) methods, respectively. The actual element contents were determined by X-ray fluorescence (XRF) technology (Axios-MAX, NEP). The micromorphology of the samples was measured by scanning electron microscopy (SEM) using an S-4800 scanning electron microscope. High-resolution transmission electron microscopy (HRTEM) images and EDS element distribution mapping were obtained on a JEM 2100F transmission electron microscope. The element binding energies (BEs) of surface species were detected by X-ray photoelectron spectroscopy (XPS) measurement using a Thermo Scientific ESCALAB 250 instrument. Temperature-programmed desorption and reaction (*e.g.* NH_3-TPD, O_2-TPD, and H_2-TPR) measurements were carried out on a Quantachrome Chemstar apparatus furnished with a thermal conductivity detector (TCD). *Ex*/*in situ* diffuse reflectance infrared Fourier-transform spectroscopy (*ex*/*in situ* DRIFTS) was analyzed on a

FTIR spectrometer (Thermo Fisher iS 50) equipped with a Harrick reaction cell. The detailed characterization procedures are described in the ESI.†

2.4 Catalytic evaluation

The activity and stability of as-synthesized $Ce_{1-x}Zr_xO_2$ and M–$Ce_{0.7}Zr_{0.3}O_2$ catalysts in the oxidation of CB and VOC mixture were tested in a temperature-controlled quartz tube reactor with 6 mm inner diameter. Typically, about 66 mg grain catalyst (40–60 mesh) was used for testing, and before filling into the reactor bed, the sample was diluted with a certain amount of quartz sand to maintain a 30 mm bed height to decrease the thermal effect during the VOC degradation process. The temperature difference was corrected through an external thermocouple installed at the bottom of the catalyst bed. In all the runs, the total flow through the reactor bed was set at 66 mL min^{-1} and the corresponding WHSV was 60 000 mL g^{-1} h^{-1}. In this work, the particle size of the catalyst (40–60 mesh) and the linear velocity of the reaction gas (3.9 cm s^{-1}) meet the requirements of overcoming the transfer barrier including internal and external transfer limitations.[5] The composition of the reaction feeding gas was 1000 ppm CB or 2000 ppm VOC mixture (1000 ppm chlorobenzene, 900 ppm benzene (B), and 100 ppm toluene (TB)), 20 vol% O_2, 0 or 5 vol% H_2O and balance N_2. The concentration of VOCs (c(VOCs)) and CO_2 ($c(CO_2)$) in the effluent gases was detected online by a FID and a TCD detector, respectively, which were installed on the gas chromatograph. The conversion (X_{VOC}) and total conversion (X_{Total}) of reactants were calculated based on the difference between the VOC concentration of the inlet and outlet gas. Mineralization (Y_{CO2}) was evaluated according to the change in CO_2 concentration. The calculation formulas are as follows:

$$X_{VOC} = \frac{c(VOC)_{Inlet} - c(VOC)_{Outlet}}{c(VOC)_{Inlet}} \times 100\% \quad (1)$$

$$X_{Total} = \frac{\sum X_{VOC} \times c(VOC)}{\sum c(VOC)} \times 100\% \quad (2)$$

$$Y_{CO_2} = \frac{c(CO_2)_{Outlet}}{c(CO_2)_{Complete}} \times 100\% \quad (3)$$

The concentration of Cl_2 in the effluent gases was determined by titration.[27] During this analysis, 50 mL of 0.0125 mol L^{-1} NaOH solution was used as an absorbent to absorb the exhaust gases at a stable CB conversion for 2 h. And then *N*,*N*-diethyl-*p*-phenylenediamine was selected as an indicator to be dropped into the solution, which would turn the solution red. 1.01 mmol L^{-1} ferrous ammonium sulfate solution was considered as a titrant to titrate the above solution rapidly until the red solution became transparent. The concentration of Cl_2 in the effluent gases can be calculated based on the consumption of ferrous ammonium sulfate solution. It should be noted that the concentration of HCl cannot be accurately determined due to the tendency of HCl to be adsorbed on the exhaust pipe (the stainless steel pipe). Moreover, it is very difficult to detect Cl atoms on trace amounts of chlorine-containing by-products or ICs deposited on the catalyst surface. Although the Cl balance during the degradation process of CB cannot be established, the quantitative measurements can reveal the trend of Cl_2 formation on each catalyst, which is sufficient to support the relevant discussion.

The degradation activity of monolithic catalyst to chlorobenzene was evaluated in a pilot-scale evaluation device. The device structure and operation process were previously reported by our group.[28] The experimental conditions were similar to those of the evaluation experiments above. The concentration of CB was 1000 ppm and the WHSV was 60 000 mL g^{-1} h^{-1}.

3. Results and discussion

3.1 Catalytic performance

3.1.1 The catalytic activity of $Ce_{1-x}Zr_xO_2$ and M–$Ce_{0.7}Zr_{0.3}O_2$ for CB degradation. By regulating the surface acidity of CeO_2 with acid sites, the $Ce_{1-x}Zr_xO_2$ and M–$Ce_{0.7}Zr_{0.3}O_2$ catalysts were prepared. According to the results of XRF, the actual acidic element loads of M–$Ce_{0.7}Zr_{0.3}O_2$ samples are all approximately 1 wt% (Table S1†). The performance of samples in CB oxidation was investigated and shown in Fig. 1. The significant difference between CB conversion and CO_2 yield is related to the formation of by-products and intermediates.[23] Among samples, pure CeO_2 and ZrO_2 show poor performance, and the complete conversion of CB cannot be achieved even if the reaction temperature reaches 560 °C. With the introduction of Lewis acid sites, the activity curves representing CB conversion and CO_2 yield significantly shift to low temperature; all binary oxides exhibit higher activity than unitary oxides. $Ce_{0.7}Zr_{0.3}O_2$ shows the optimal activity in catalytic combustion of CB among these binary oxides. After acid element modification, the activity of $Ce_{0.7}Zr_{0.3}O_2$ was further improved. As expected, the presence of Brønsted acid sites is conducive to the degradation of CB. By taking both values of T_{90} (the temperature where 90% CB conversion or CO_2 yield is achieved) for CB conversion and mineralization into account, S–$Ce_{0.7}Zr_{0.3}O_2$ is considered as an optimal catalyst and shows higher activity (406 °C for CB conversion and 419 °C for CO_2 yield) than other acid-modified samples. Based on the results of activity tests, CeO_2, $Ce_{0.7}Zr_{0.3}O_2$, and S–$Ce_{0.7}Zr_{0.3}O_2$ catalysts were selected as representatives for subsequent research. It needs to be mentioned that the successful introduction of Lewis and Brønsted acid sites through Zr doping and sulfur modification have been confirmed by subsequent multiple characterization measurements (NH_3-TPD, pyridine-DRIFTS, and NH_3-DRIFTS).

3.1.2 The chlorine tolerance, water resistance, and Cl_2 selectivity of selected samples in CB degradation. The anti-toxicity of materials was tested at specific temperatures of around T_{90}. As shown in Fig. 2a, the CB conversion of CeO_2

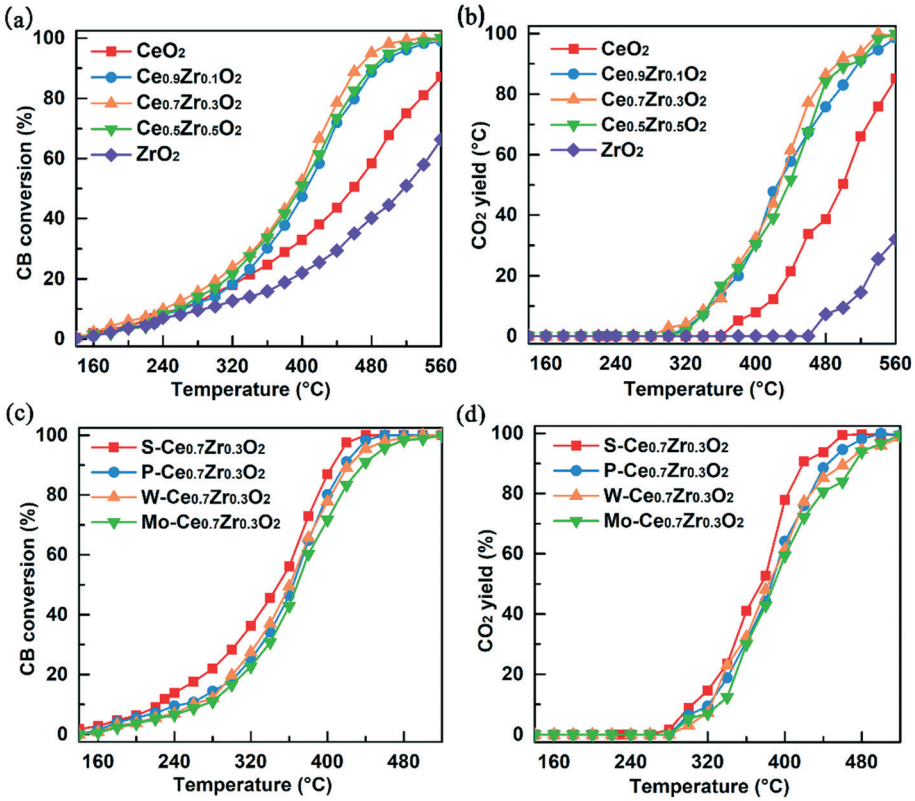

Fig. 1 CB conversion and CO_2 yield curves of (a and b) $Ce_{1-x}Zr_xO_2$ and (c and d) M–$Ce_{0.7}Zr_{0.3}O_2$ under experimental conditions: *c*(CB) = 1000 ppm, WHSV = 60 000 mL g^{-1} h^{-1}.

decreased sharply from 90% to 75% within 24 h of reaction time, showing a significant deactivation. In particular, poor performance is associated with Cl poisoning caused by the formation of Ce–Cl.[28] For $Ce_{0.7}Zr_{0.3}O_2$ and S–$Ce_{0.7}Zr_{0.3}O_2$, an excellent anti-inactivation ability can be observed; the conversion is maintained at about 90% for at least 24 h. It is established that Cl deposition on the surface of two samples is inhibited by the acid sites. The selectivity of Cl_2 during CB oxidation over three catalysts was detected at the same CB conversion (Fig. 2b). To minimize experimental errors, a relatively high CB conversion (~90%) was selected and the reaction temperatures were controlled close to T_{90} of the three catalysts. As expected, the introduction of Lewis acid accelerated the Deacon reaction and promoted the fracture of the Ce–Cl bond, resulting in more Cl_2 production (15.0%) on the surface of $Ce_{0.7}Zr_{0.3}O_2$. Due to the presence of abundant Brønsted acid sites, the degradation of CB on the S–$Ce_{0.7}Zr_{0.3}O_2$ catalyst follows the hydrolysis route, leading to minimal Cl_2 selectivity (1.2%).

The effect of water vapor on the catalytic properties of samples for CB degradation was explored (Fig. 2c and d). After 5 vol% water vapor was introduced into the reaction stream, both CB conversion and CO_2 yield of the three samples decreased to some extent due to the competitive adsorption of H_2O and CB or intermediates on the activity sites. With the increase of the reaction temperature, the activity curves of S–$Ce_{0.7}Zr_{0.3}O_2$ at different humidity are gradually close or even coincident, indicating that the effect of water is fading away. However, even when the temperature reached 560 °C, significant competitive adsorption can be observed on the activity curves of CeO_2 and $Ce_{0.7}Zr_{0.3}O_2$. On the other hand, the difference between CB conversion and CO_2 yield decreased strikingly for all the samples. In particular, for S–$Ce_{0.7}Zr_{0.3}O_2$, the activity curves of conversion and mineralization almost overlap. As described earlier, the concentration of intermediates and reactants on the material surface results in lower values of CO_2 yield than reactant conversion. With the occurrence of competitive adsorption, the adsorption sites were occupied by water molecules, which inhibited the accumulation of intermediates and made the conversion and mineralization tend to be consistent. Based on the values of T_{90}, it can be seen that the activity of S–$Ce_{0.7}Zr_{0.3}O_2$ at high temperature is greatly maintained in the presence of 5 vol% water vapor. The abundant Brønsted acid sites (–OH) of the sample can be used to explain this phenomenon in terms of competitive adsorption and reaction pathway. The hydroxy group has a higher affinity for water molecules, which can protect Lewis acid sites from being poisoned by water molecules to a certain extent and preserve the redox sites of the catalyst. Moreover, the abundance of the hydroxy group would change the degradation pathway of CB, and the initial step of the reaction is transformed from oxidation to hydrolysis, which can be accelerated by water vapor.[22,29] A detailed discussion

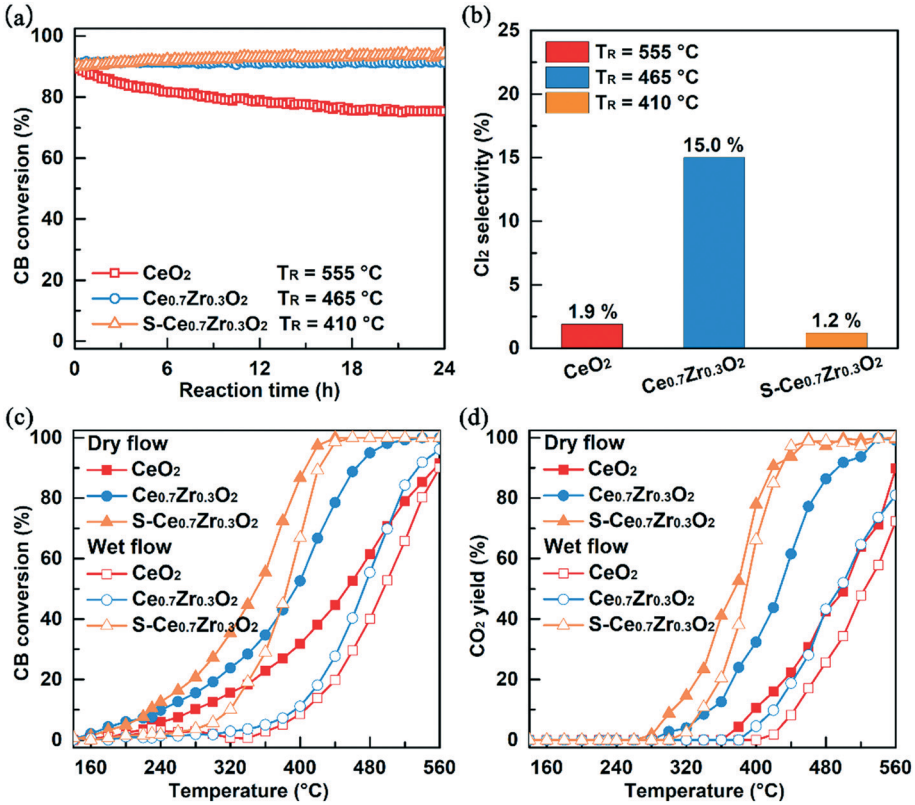

Fig. 2 (a) Anti-toxicity test and (b) Cl_2 selectivity during CB oxidation of CeO_2, $Ce_{0.7}Zr_{0.3}O_2$, and S–$Ce_{0.7}Zr_{0.3}O_2$ catalysts under experimental conditions: *c*(CB) = 1000 ppm, WHSV = 60 000 mL g^{-1} h^{-1}, H_2O content = 0 vol%; (c) CB conversion and (d) CO_2 yield curves over CeO_2, $Ce_{0.7}Zr_{0.3}O_2$, and S–$Ce_{0.7}Zr_{0.3}O_2$ catalysts in the absence or presence 5 vol% H_2O under experimental conditions: *c*(CB) = 1000 ppm, WHSV = 60 000 mL g^{-1} h^{-1}.

about the reaction pathway of different samples will be conducted in the *in situ* DRIFTS analysis.

3.1.3 The distribution of by-products. The distribution of by-products produced by CB chlorination can more intuitively reflect the environmental risk of the three catalysts. Within the limitation of the FID, only three isomers of dichlorobenzene (DCB), including *o*-DCB, *m*-DCB, and *p*-DCB, were detected. Because of the different catalytic activities of the three samples, the temperature range of the distribution of by-products were different, but the law were similar and the distribution curves all show a volcanic shape (Fig. 3). For the CeO_2 sample, all three isomers were detected in the effluent gas of CB degradation until the reaction temperature reached 560 °C. With the introduction of Zr ions, the distribution curves of DCB shifted to a lower temperature range, and the maxima of concentration about *o*-DCB (21 ppm) and *p*-DCB (15 ppm) increase significantly. The increase of Lewis acid sites can improve the CB degradation

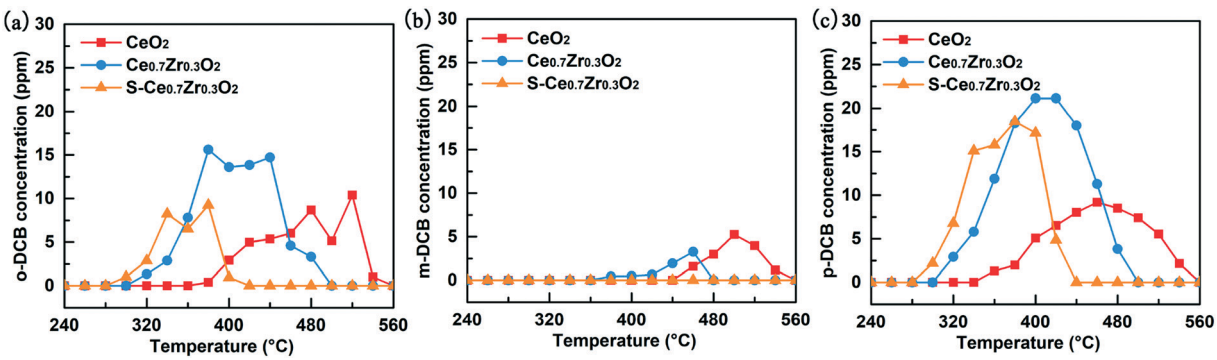

Fig. 3 DCB distributions for CB combustion over CeO_2, $Ce_{0.7}Zr_{0.3}O_2$, and S–$Ce_{0.7}Zr_{0.3}O_2$ catalysts under experimental condition: *c*(CB) = 1000 ppm, WHSV = 60 000 mL g^{-1} h^{-1}, H_2O content = 0 vol%; (a) *o*-DCB; (b) *m*-DCB; and (c) *p*-DCB.

performance of the catalyst; however, it would also promote the generation of more chlorinated by-products and bring greater environmental risks. Compared with $Ce_{0.7}Zr_{0.3}O_2$, the DCB distribution curves of S–$Ce_{0.7}Zr_{0.3}O_2$ had a narrower temperature range and a smaller value of maximum concentration, and even the generation of *m*-DCB was not detected in the whole process. It is obvious that the introduction of Brønsted acid sites can effectively inhibit the formation of chlorination by-products, which is consistent with the expectation.

3.1.4 The catalytic stability of S–$Ce_{0.7}Zr_{0.3}O_2$. Stability test and cycling tests were performed to investigate the durability of S–$Ce_{0.7}Zr_{0.3}O_2$ under 5 vol% water vapor. As depicted in Fig. 4a, when the reaction temperature is maintained at 420 °C, approximately 89% CB conversion and 84% CO_2 yield could be achieved and maintained for more than 100 h. During the 106 hours test, the CB conversion and CO_2 yield at the corresponding temperature are consistent with the data of the activity test, and no evident deactivation was detected. This encouraging result demonstrates the high stability of S–$Ce_{0.7}Zr_{0.3}O_2$ in the degradation of CB. According to previous literature, HCl in the reaction flow may lead to the reduction of sulfur species on the surface, and even Moser *et al.* used a diluted HCl stream to regenerate sulfur poisoning catalysts.[30] As discussed earlier, the presence of sulfur element on the surface is critical to the excellent catalytic performance of S–$Ce_{0.7}Zr_{0.3}O_2$. Therefore, the retention value of sulfur content after the reaction is also an important factor to evaluate the stability of S–$Ce_{0.7}Zr_{0.3}O_2$. The retained amount of sulfur element on the sample after the long-term stability test was determined by XRF characterization and shown in Fig. 4a. Similar to the report of Moser *et al.*, the sulfur content on the surface of the used sample was reduced to some extent.[30] However, due to the strong adsorption of sulfur on $Ce_{0.7}Zr_{0.3}O_2$, 73.5% of the sulfur element was still retained even after 106 h of reaction. It was interesting to see that even though the sulfur content was reduced, S–$Ce_{0.7}Zr_{0.3}O_2$ retained the initial activity in the long-term stability test. It could be assumed that the improvement of catalytic performance of S–$Ce_{0.7}Zr_{0.3}O_2$ mainly comes from the sulfur species strongly adsorbed on $Ce_{0.7}Zr_{0.3}O_2$, which is almost not affected by the toxicity of HCl. Moreover, the effect of the reaction cycle on the redox properties and acidity of S–$Ce_{0.7}Zr_{0.3}O_2$ may also be responsible for its excellent stability, which would be discussed below. In Fig. 4b and c, the activity curves of both conversion and mineralization are almost unchanged after six activity cycles, which also confirmed the high stability of the S–$Ce_{0.7}Zr_{0.3}O_2$ catalyst for CB combustion.

3.1.5 The adaptability of S–$Ce_{0.7}Zr_{0.3}O_2$ under near-real conditions. To evaluate the application potential of S–$Ce_{0.7}Zr_{0.3}O_2$ under near-real conditions, degradation tests of a VOC mixture on S–$Ce_{0.7}Zr_{0.3}O_2$ were performed in the presence 5 vol% water vapor. As shown in Fig. 5a, the

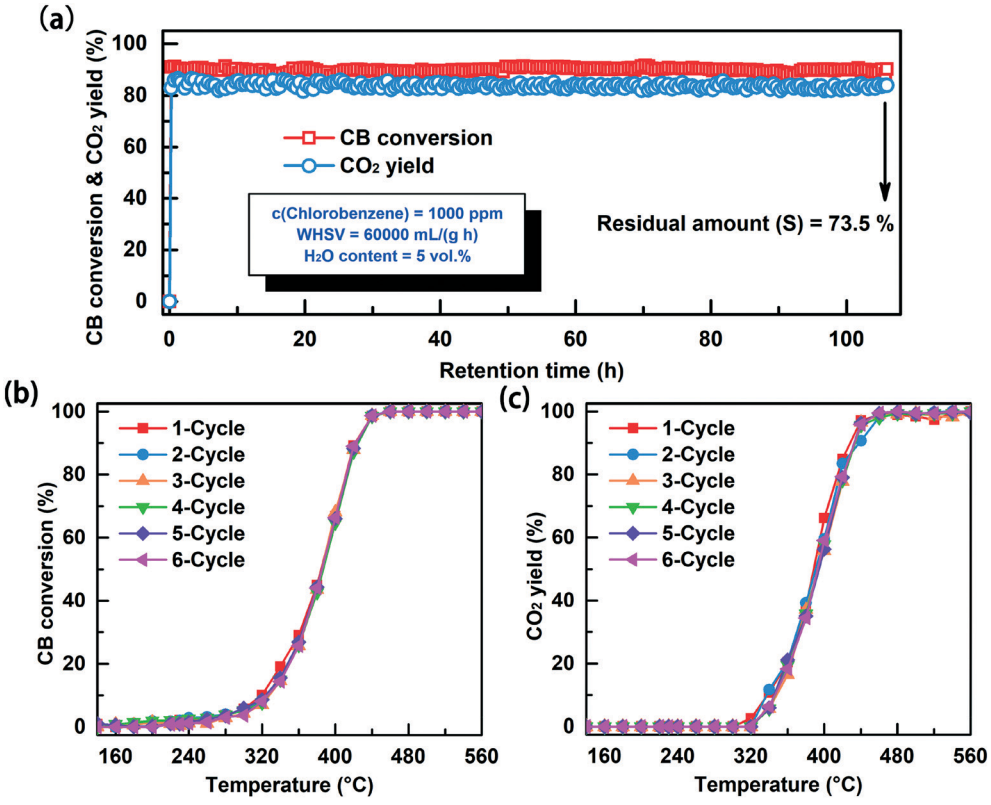

Fig. 4 (a) Long-term stability test of S–$Ce_{0.7}Zr_{0.3}O_2$ in catalytic oxidation of CB at 420 °C and (b and c) cycling stability tests of S–$Ce_{0.7}Zr_{0.3}O_2$ in catalytic oxidation of CB under experimental conditions: *c*(CB) = 1000 ppm, WHSV = 60 000 mL g^{-1} h^{-1}, H_2O content = 5 vol%.

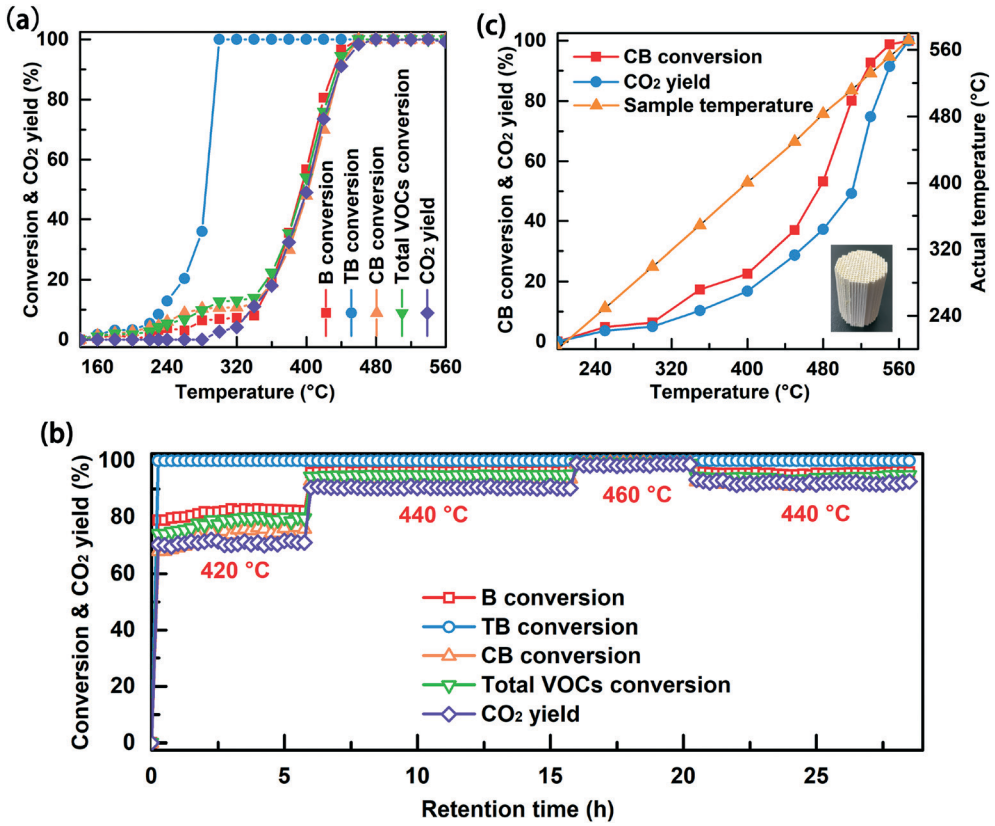

Fig. 5 (a) Activity curves and (b) long-term stability test of S–$Ce_{0.7}Zr_{0.3}O_2$ in catalytic oxidation of the VOC mixture under experimental conditions: *c*(VOCs mixture) = 2000 ppm (1000 ppm CB, 900 ppm B, and 100 ppm TB), WHSV = 60 000 mL g^{-1} h^{-1}, H_2O content = 5 vol%; (c) catalytic activity test of the monolithic catalyst for CB under experimental conditions: *c*(CB) = 1000 ppm, WHSV = 60 000 mL g^{-1} h^{-1}.

catalytic activity of the sample for CB oxidation was remarkably maintained and almost complete conversion of the VOC mixture can be achieved at a reaction temperature of 460 °C. Moreover, the S–$Ce_{0.7}Zr_{0.3}O_2$ catalyst presented excellent long-term stability and evident deactivation was still not detected within 28.5 hours of observation (Fig. 5b). In practical industrial applications, more attention is paid to the catalytic performance of monolithic catalysts with high mechanical strength and low pressure drop, which are more suitable for harsh working conditions. Therefore, a monolithic catalyst was prepared to degrade CB by loading S–$Ce_{0.7}Zr_{0.3}O_2$ powder onto a cylindrical cordierite honeycomb ceramic. The activity test was performed in a pilot-scale evaluation device using ambient air as the feed gas (Fig. 5c). According to the data, the relative humidity in the environmental atmosphere on the test day was 75%, equivalent to about 3 vol% water at 25 °C. To ensure the accuracy of the test, a thermocouple was placed near the integral catalyst to correct the temperature difference. Affected by some unfavorable factors, such as low load, uneven coating, and poor contact efficiency, a significant decrease in the activity of the monolithic catalyst was observed, which has been found in previous research.[28] Even so, the monolithic catalyst was able to achieve a CB conversion of over 98% at 550 °C, which is acceptable for regenerative catalytic oxidation (RCO).

3.2 Catalyst characterization

3.2.1 Morphology, pore structure, surface area, and crystal phase. The microstructure of samples was observed through SEM. As shown in Fig. 6a–f, it is obvious that all samples show a high-quality 3DOM structure; even after acid modification, the 3DOM skeleton structure of the samples is completely maintained. The periodic voids in the long-range ordered architecture are interconnected through open windows with a macropore diameter of 340–420 nm. Moreover, the multi-layered structure is highly visible. The three-dimensional macroporous architecture with a high degree of ordered arrangement provides a convenient channel for reactants and products to diffuse within the catalysts.[31] In addition, the SEM images of used samples were also collected (Fig. S1†). Notably, the used samples still showed a good three-dimensional ordered structure, indicating the good mechanical stability of the samples. The BET surface areas of the materials are listed in Table 1. The data show that the as-prepared materials of CeO_2 (63.4 m^2 g^{-1}) and $Ce_{0.7}Zr_{0.3}O_2$ (79.8 m^2 g^{-1}) both have a relatively large specific surface area, which is beneficial for the homogeneous dispersion of sulfur element. The S–$Ce_{0.7}Zr_{0.3}O_2$ sample displayed a lower surface area (53.7 m^2 g^{-1}) than $Ce_{0.7}Zr_{0.3}O_2$, a result possible because of the destruction of some micropores during modification. To examine whether

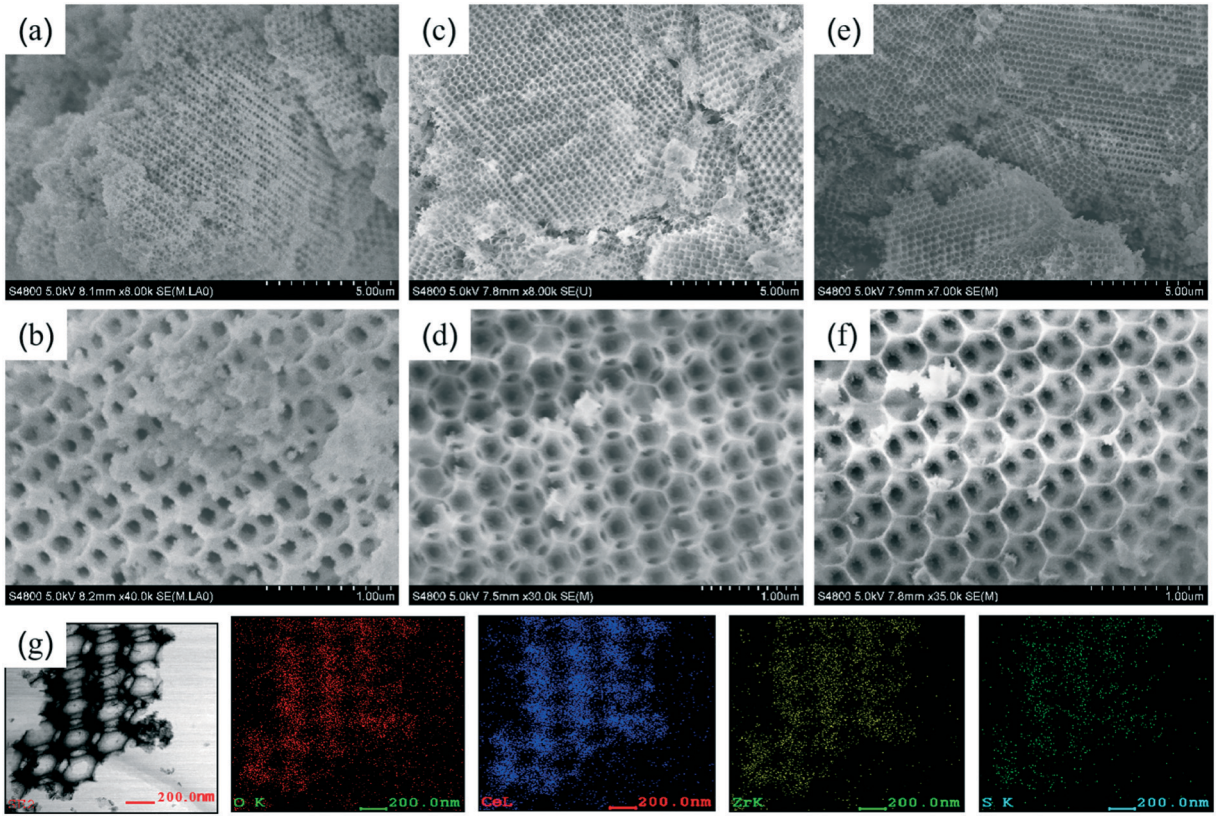

Fig. 6 SEM images of (a and b) CeO_2, (c and d) $Ce_{0.7}Zr_{0.3}O_2$ and (e and f) S–$Ce_{0.7}Zr_{0.3}O_2$. (g) EDS element mapping images of S–$Ce_{0.7}Zr_{0.3}O_2$.

the sulfur element is uniformly grafted onto the surface of $Ce_{0.7}Zr_{0.3}O_2$, EDS elemental mapping images of the S–$Ce_{0.7}Zr_{0.3}O_2$ sample were collected. As shown in Fig. 6g, it can be confirmed that sulfur is evenly distributed throughout the skeleton surface, which meets the experimental expectation.

The crystal structure of the samples was investigated by XRD and HRTEM characterization. As described in Fig. 7a, the spectra of the three samples are all similar. For the CeO_2 sample, several diffraction peaks appeared at 28.6°, 33.1°, 47.5°, 56.4°, 59.1°, 69.4°, 76.7°, 79.1°, and 88.5°, which are assigned to the (111), (200), (220), (311), (222), (400), (331), (420), and (422) lattice planes of cubic fluorite CeO_2 (PDF#00-043-1002), respectively. With the addition of Zr ions, the diffraction peaks become weak and migrate to the higher angle, indicating that the lattice distortion is caused by the formation of Ce–O–Zr solid solution.[32,33] In addition, no impurity peak in the XRD patterns of S–$Ce_{0.7}Zr_{0.3}O_2$ sample was observed, indicating that the sulfur element is highly dispersed or exists in the amorphous phase. As shown in Fig. 7b–d, well-resolved lattice fringes can be observed in the HRTEM images of the three selected samples. For the CeO_2 sample, the lattice spacings were measured to be 0.106, 0.193, 0.265, and 0.309 nm, which belong to the (422), (220), (200), and (111) planes of the standard CeO_2 sample, respectively. As Zr ions with small ionic radius enter the lattice of the CeO_2 material, the lattice spacing of the $Ce_{0.7}Zr_{0.3}O_2$ sample becomes wider.[34] Moreover, a further increase in lattice spacing is associated with electron transfer of Ce–O to S–O after sulfur modification.[35] Similar to the XRD analysis, no crystal planes associated with ZrO_2 or sulfur element were observed. To investigate the stability of the crystal phase structure of the samples, the XRD patterns (Fig. S3a†) of the used three samples and the HRTEM image (Fig. S3b†) of the used S–$Ce_{0.7}Zr_{0.3}O_2$ were observed. It is gratifying that the crystal phase structure of the samples did not change significantly after the reaction.

3.2.2 Surface element composition and chemical state. The chemical states of Ce, Zr, and S on the surface of the catalysts were probed *via* XPS (Fig. 8). The spectra of Ce 3d can be fitted into nine peaks, the binding energies of 882.3–882.5, 888.7–888.8, 897.7–897.9, 900.8–900.9, 907.4–907.5, and 916.5–916.7 eV are associated with Ce^{4+}, and those of 884.7–885.3, 898.5–898.6, and 902.7–903.0 eV are associated with Ce^{3+}.[36] For each sample, cerium exists on the surface in a mixed oxidation state of Ce^{3+} and Ce^{4+}, where Ce^{3+} is generally considered to be related to the formation of oxygen vacancies.[37] The Ce^{4+}/Ce^{3+} molar ratios of three samples are calculated by the corresponding peak areas and listed in Table 1. It can be found that the content of Ce^{3+} in the catalyst increases with the introduction of high valent Zr ions. This result is associated with the increase of oxygen vacancies caused by lattice distortion. After sulfur modification, the increase of Ce^{4+} concentration is related to electron transfer of Ce–O to S–O.[35,38] Compared to metal

Table 1 Summary of physicochemical characteristics and activity data

Catalyst	BET surface area ($m^2\ g^{-1}$)	Macropore diameter[a] (nm)	XPS		$A_B{}^b/A_L{}^c$		$T_{50}{}^d$ (°C)			T_{90} (°C)		
			O_{latt}/O_{ads}	Ce^{4+}/Ce^{3+}	Pyridine-DRIFTS	NH_3-DRIFTS	CB conversion	CO_2 yield	ΔT^e	CB conversion	CO_2 yield	ΔT^e
CeO_2	63.4	340–390	1.94	2.72	0.172	1.123	453	501	48	555	—	—
$Ce_{0.7}Zr_{0.3}O_2$	79.8	380–420	2.35	2.67	0.095	0.866	390	427	37	464	493	29
S–$Ce_{0.7}Zr_{0.3}O_2$	53.7	380–420	1.91	3.02	0.210	2.100	348	374	26	406	419	13
CeO_2-wet	—	—	—	—	—	—	496	524	28	560	—	—
$Ce_{0.7}Zr_{0.3}O_2$-wet	—	—	—	—	—	—	473	495	22	535	—	—
S–$Ce_{0.7}Zr_{0.3}O_2$-wet	—	—	—	—	—	—	385	388	3	422	428	6

[a] Data were obtained according to the SEM images. [b] A_B is the total area of the peaks corresponding to the Brønsted acid in the spectra of pyridine-DRIFTS or NH_3-DRIFTS. [c] A_L is the total area of the peaks corresponding to the Lewis acid in the spectra of pyridine-DRIFTS or NH_3-DRIFTS. [d] The temperature where 50% CB conversion or CO_2 yield was achieved. [e] ΔT is the temperature difference between T_{50} or T_{90} of CB conversion and CO_2 yield.

ions, sulfur is more electronegative and has a greater ability to attract electrons.[10] For the samples containing Zr ions, the spectra are divided into two peaks at 182.0–182.4 and 184.4–184.6 eV, which are assigned to Zr $3d_{5/2}$ and Zr $3d_{3/2}$ of Zr^{4+} species, respectively.[39] The spectrum of S 2p can be fitted by two peaks with the binding energies of 168.7 and 169.9 eV attributed to S $2p_{3/2}$ in S(VI) species, which suggests the existence of $SO_4{}^{2-}$ on the surface of S–$Ce_{0.7}Zr_{0.3}O_2$.[40] Other forms of the sulfur element such as sulfide, elemental sulfur or sulfite were not observed. Moreover, the spectra of O 1s, Ce 3d, Zr 3d, and S 2p of the used samples were also collected *via* XPS characterization (Fig. S4†). The spectra of Ce 3d were fitted and processed in a similar manner to those of fresh catalysts, and the Ce^{4+}/Ce^{3+} molar ratios of the used samples are listed in Table S2.† After a reaction cycle, the proportion of Ce^{3+} on the surface of all samples was increased, which may mean an increase in oxygen vacancy. With the occurrence of CB oxidation, the reactive oxygen species on the surface of the catalysts were constantly consumed, and the formation of oxygen vacancies was almost an inevitable result.[41] As shown in Fig. S4b and c,† the Zr and S elements still exist in the form of Zr^{4+} and $SO_4{}^{2-}$, and no other chemical states appear. The O 1s spectra of the used samples would be discussed in detail in the next section.

3.2.3 Oxygen species and low-temperature reducibility. The surface reactive oxygen species of the samples were evaluated by XPS and O_2-TPD. As shown in Fig. 9a, the O 1s XPS spectra for all samples can be decomposed to two peaks, centered at regions of 529.4–529.6 eV and 531.4–531.7 eV, and ascribed to lattice oxygen (O_{latt}) and surface adsorbed oxygen (O_{ads}), respectively.[42] Based on the integral ratio of O_{latt} to O_{ads} listed in Table 1, the activation of lattice oxygen by Zr incorporation is found. This phenomenon can be attributed to lattice distortion as the Zr ions enter into the lattice of CeO_2, which has been found by XRD and HRTEM analysis. On the other hand, the decrease of the proportion of active lattice oxygen on the surface of S–$Ce_{0.7}Zr_{0.3}O_2$ is due to the coverage of sulfur element.[28] In fact, only surface active oxygen species of the samples can be obtained through the XPS spectra of O 1s; however, the overall composition of bulky oxygen species in the catalyst needs to be further confirmed by O_2-TPD (Fig. 9b). In general, the oxygen desorption peak consists of three regions, namely the low temperature region (<300 °C), the medium temperature region (300–400 °C), and the high temperature region (>400 °C), corresponding to the physical adsorption oxygen, chemical adsorption oxygen or surface lattice oxygen and bulk lattice oxygen, respectively.[43] As shown in Fig. 9b, the O_2-TPD profile of the CeO_2 sample has a strong peak below 300 °C, which is correlated to the desorption of O_2 weakly adsorbed on the surface. For higher temperature regions, especially in the range of 300–400 °C, desorption of O_2 is almost nonexistent, meaning a very small amount of active lattice oxygen. For $Ce_{0.7}Zr_{0.3}O_2$ sample, the positive effect of Zr doping on surface reactive oxygen species is obvious, and

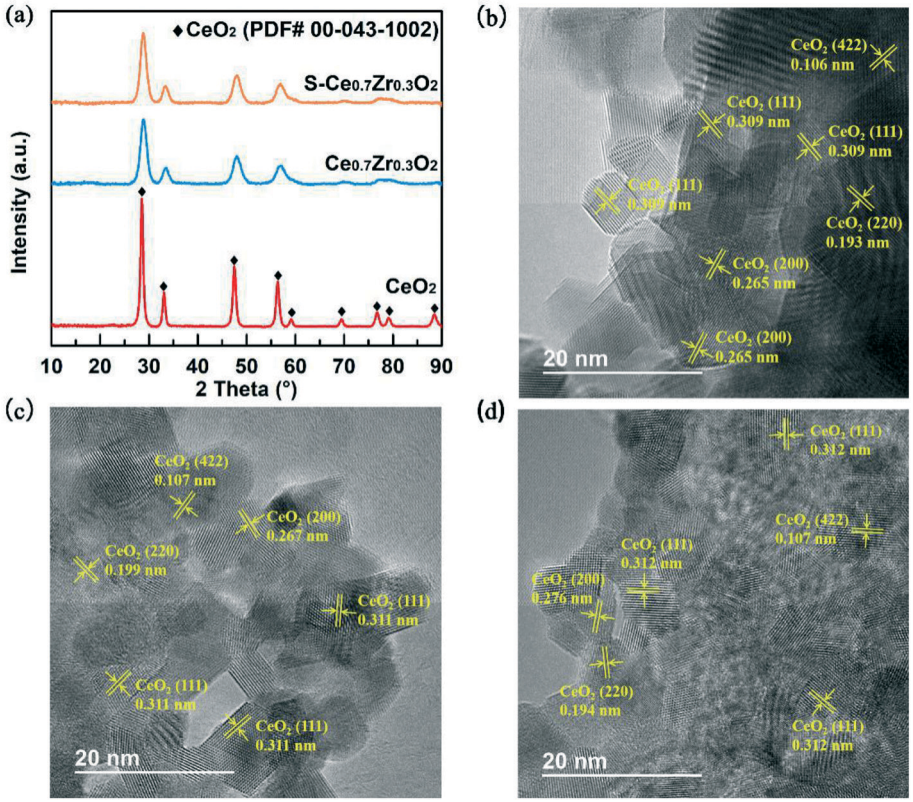

Fig. 7 (a) XRD patterns of samples and HRTEM images of (b) CeO_2, (c) $Ce_{0.7}Zr_{0.3}O_2$, and (d) S–$Ce_{0.7}Zr_{0.3}O_2$.

the desorption of O_2 is observed throughout the temperature range. It should be mentioned that the increase in the concentration of surface active lattice oxygen is important for the catalytic performance of the catalyst. As we all know, the oxidation reaction of VOCs on the catalyst generally follows the Mars–van-Krevelen (MVK) mechanism, with the active lattice oxygen playing a critical role.[44] Abundant active lattice oxygen species are the source of the better catalytic performance of $Ce_{0.7}Zr_{0.3}O_2$ than CeO_2. In the profile of the S–$Ce_{0.7}Zr_{0.3}O_2$ sample, the desorption peak at the low temperature region becomes weaker when incorporating SO_4^{2-}, correlated with the coverage of sulfur element on the $Ce_{0.7}Zr_{0.3}O_2$ surface.[28] The new desorption peak that appears in the high temperature region of S–$Ce_{0.7}Zr_{0.3}O_2$ sample is attributed to the decomposition of SO_4^{2-} rather than the desorption of lattice oxygen.[45]

The low temperature reducibility of samples is closely related to its catalytic performance, which is investigated through H_2-TPR. As shown in Fig. 9c, the pristine CeO_2 presents two reduction peaks at 407 and 514 °C, in which the former is attributed to the consumption of surface chemisorption oxygen species (O_{ads}), whereas the latter is associated with the reduction of the lattice oxygen species (O_{latt}).[46,47] For the $Ce_{0.7}Zr_{0.3}O_2$ sample, the peak ascribed to

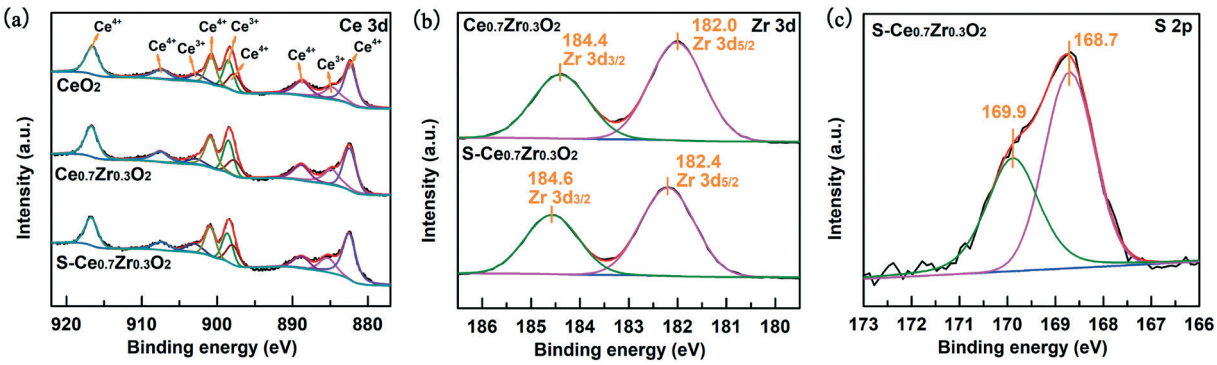

Fig. 8 (a) Ce 3d XPS spectra of CeO_2, $Ce_{0.7}Zr_{0.3}O_2$, and S–$Ce_{0.7}Zr_{0.3}O_2$; (b) Zr 3d XPS spectra of $Ce_{0.7}Zr_{0.3}O_2$, and S–$Ce_{0.7}Zr_{0.3}O_2$; and (c) S 2p XPS spectra of S–$Ce_{0.7}Zr_{0.3}O_2$.

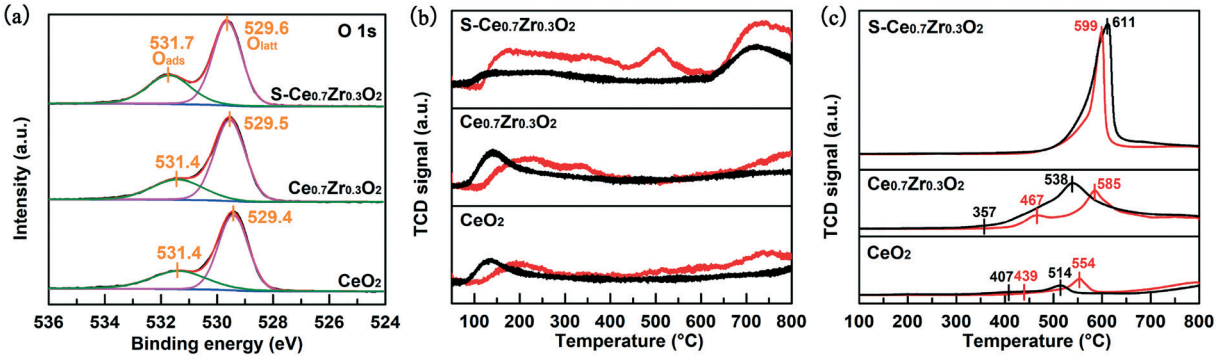

Fig. 9 (a) O 1s XPS spectra of fresh CeO_2, $Ce_{0.7}Zr_{0.3}O_2$, and S–$Ce_{0.7}Zr_{0.3}O_2$; (b) O_2-TPD profiles; and (c) H_2-TPR profiles of fresh (black lines) and used (red lines) CeO_2, $Ce_{0.7}Zr_{0.3}O_2$, and S–$Ce_{0.7}Zr_{0.3}O_2$.

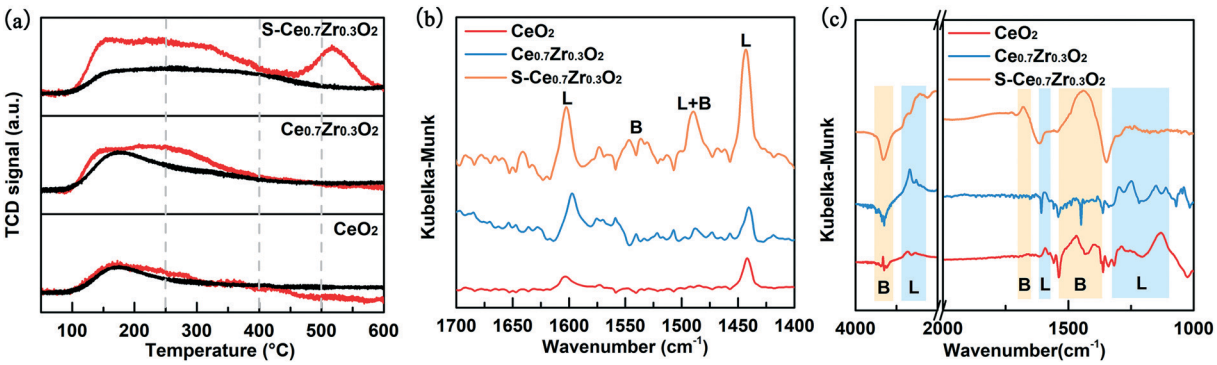

Fig. 10 (a) NH_3-TPD profiles of fresh (black lines) and used (red lines) CeO_2, $Ce_{0.7}Zr_{0.3}O_2$, and S–$Ce_{0.7}Zr_{0.3}O_2$; (b) pyridine-DRIFTS spectra and (c) NH_3-DRIFTS spectra of fresh CeO_2, $Ce_{0.7}Zr_{0.3}O_2$, and S–$Ce_{0.7}Zr_{0.3}O_2$.

reduction of O_{ads} shifted to a lower temperature (357 °C), reflecting better reducibility of the sample, which is related to the lattice distortion. It is interesting to note that the second peak of $Ce_{0.7}Zr_{0.3}O_2$ shifted towards higher temperatures (538 °C). However, it is not reasonable to conclude that the reducibility of the sample is limited after Zr doping, as the peak intensity of $Ce_{0.7}Zr_{0.3}O_2$ is much higher than that of CeO_2. The higher temperature of the second peak is associated with more bulk lattice oxygen species being involved in the reduction process. The outstanding low temperature reducibility is the intrinsic reason for the activity improvement of $Ce_{0.7}Zr_{0.3}O_2$. After the modification of sulfur element, the reduction peak shifted to high temperature greatly, which is probably due to the stabilizing effect of SO_4^{2-} combined with Zr ions.[48] The abnormally large peak area is due to the reduction in S(VI) species to yield H_2S and/or SO_2.[49] Based on the results of O_2-TPD and H_2-TPR, it can be clearly found that the significant improvement of catalytic activity caused by acid modification cannot be well demonstrated from the perspective of active lattice oxygen and low temperature reducibility. According to the literature, the difference of acid sites may play a key role in the change of the activity.[6,23,50]

Although it does not play a leading role in CB oxidation, the comparison of redox properties of samples before and after the reaction is conducive to a deeper understanding of the whole degradation process. According to the MVK mechanism, the degradation process of CB on the catalyst surfaces involves the consumption and supplementation of reactive oxygen species.[41] In the initial stage of the reaction, the consumption rate of reactive oxygen species is often higher than the replenishment rate, which leads to the increase of oxygen vacancies on the surfaces. It is almost universally acknowledged that a modest increase in oxygen vacancies is conducive to the activation and migration of lattice oxygen.[43] It can be seen from the O_2-TPD profiles that the amount of lattice oxygen desorption from the used samples all increased significantly. Furthermore, the integral ratios of surface O_{latt} to O_{ads} obtained from O 1s spectra of fresh and used (Table S2†) samples were compared. Analogously, the proportions of lattice oxygen on the used samples' surface were significantly increased. In fact, CB can be regarded as a reductive gas, and the whole reaction process is similar to a pre-reduction treatment of the samples. Therefore, the low temperature reducibility of the used samples was generally poorer than that of the fresh samples, and the peaks of H_2-TPR all shifted to a higher temperature. It is worth noting that oxygen vacancy is a form of Lewis acid. Therefore, it can be inferred that the acidity of the used samples, especially Lewis acids, would be enhanced.

3.2.4 Acid properties. NH_3-TPD, pyridine-DRIFTS, and NH_3-DRIFTS measurements were used to evaluate the acid properties of catalysts. The concentration of surface acid sites on the samples was detected by NH_3-TPD. Considering the interference of decomposed SO_4^{2-}, the experiments were carried out in the range of 50–600 °C. As shown in Fig. 10a, the NH_3 desorption curves of the samples can be divided into four temperature ranges: <250 °C, 250–400 °C, 400–500 °C, and >500 °C, representing weak, moderate, strong and super-strong acid, respectively.[10] For CeO_2 and $Ce_{0.7}Zr_{0.3}O_2$, the desorption of NH_3 occurs intensively below 400 °C, indicating that the acid sites of the samples are mainly weak and medium acid sites, with almost no strong acid sites. Compared with CeO_2, the introduction of high valence Zr ions promotes the formation of Lewis acid and increases the content of acid sites on the surface of $Ce_{0.7}Zr_{0.3}O_2$.[51] Moreover, the enhancement of acid strength on the catalyst by sulfur-grafting was also observed. For the S–$Ce_{0.7}Zr_{0.3}O_2$ sample, in addition to abundant medium–strong acid sites, desorption of NH_3 above 500 °C occurs, which verifies the existence of super-strong acid. Compared to the weak acid, the stronger acid is commonly beneficial to activation of CVOCs.[8] The obvious advantage in acidity leads to the excellent catalytic activity of S–$Ce_{0.7}Zr_{0.3}O_2$ for CB oxidation.

On pyridine-DRIFTS spectra (Fig. 10b) of CeO_2, $Ce_{0.7}Zr_{0.3}O_2$, and S–$Ce_{0.7}Zr_{0.3}O_2$ samples evacuated at 120 °C, the bands at 1602, 1559–1522, 1490, and 1443 cm^{-1} are observed. The bands at 1602 and 1443 cm^{-1} are assigned to the Lewis acid;[4] the bands in the range of 1559–1522 cm^{-1} are associated with the Brønsted acid; and the band representing the coordination bound pyridine to both Brønsted and Lewis acid sites at 1490 cm^{-1} is related to total acidity.[52] The spectra of NH_3-DRIFTS are exhibited in Fig. 10c. The reverse band at 3627 cm^{-1} and the bands in the region of 1500–1400 cm^{-1} are ascribed to NH^{4+} adsorption on surface acid hydroxyl (Brønsted acid). The bonds at 1678 cm^{-1} over the S–$Ce_{0.7}Zr_{0.3}O_2$ sample correspond to Brønsted acid sites. The peaks in the range of 3432–3113 cm^{-1} originated from stretching vibrations of NH_3 adsorbed on Lewis acid sites. In addition, the other peaks at 1592 cm^{-1} and 1323–1074 cm^{-1} are attributed to NH_3 adsorbed on Lewis acid sites.[19] According to the strength difference of each peak, the change of acidity on the catalyst surface is consistent with the assumption. In order to accurately reflect the distribution of different types of acid sites, the total area ratios of the peaks corresponding to Brønsted and Lewis acid sites (A_B/A_L) were calculated and listed in Table 1. Because of the different adsorption tendencies of pyridine and NH_3 on two types of acid sites, the values of A_B/A_L based on the spectra of pyridine-DRIFTS and NH_3-DRIFTS are quite different. However, the patterns of these values are similar for the three catalysts. With the addition of Zr ions into CeO_2, the values of A_B/A_L significantly decrease, representing an increase in the proportion of Lewis acid sites on the material surface. The maximum values of A_B/A_L indicate that the surface of S–$Ce_{0.7}Zr_{0.3}O_2$ is rich in Brønsted acid sites. Similar conclusions can be drawn from the analysis of two types of adsorption spectra. Lewis and Brønsted acid sites were successfully introduced into the 3DOM skeleton of catalyst by Zr doping and sulfur grafting, respectively.

As mentioned earlier, it is possible for the acidity of the used samples to be enhanced through a reaction cycle. To explore the effect of the reaction process on the surface acidity of the samples, NH_3-TPD and NH_3-DRIFTS measurements of the used samples were performed. For $Ce_{0.7}Zr_{0.3}O_2$ and S–$Ce_{0.7}Zr_{0.3}O_2$, the concentration of surface acid sites greatly increased as predicted. The surface acidity of S–$Ce_{0.7}Zr_{0.3}O_2$ was enhanced most obviously, and even a large number of super-strong acid sites appeared. During the reaction process, some sulfur species weakly adsorbed on $Ce_{0.7}Zr_{0.3}O_2$ desorbed from the surface under the effect of HCl, resulting in the exposure of abundant oxygen vacancies. As a result, the surface acidity of S–$Ce_{0.7}Zr_{0.3}O_2$ increased despite the decrease in the amount of surface sulfur. This may be the essential reason for the excellent stability of S–$Ce_{0.7}Zr_{0.3}O_2$. In particular, although the oxygen vacancy concentration of CeO_2 increased, its acidity was inhibited. The Cl ions deposited on the surface of CeO_2 occupied the surface acid sites. It is worth mentioning that the introduction of both Lewis and Brønsted acids can effectively inhibit the deposition of Cl ions at active sites, which had been confirmed in the anti-toxicity test. Therefore, the acidity

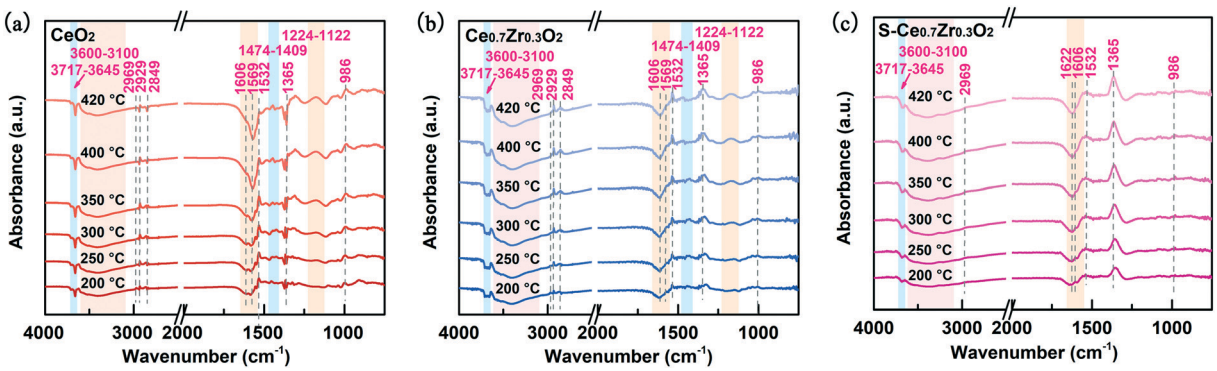

Fig. 11 *In situ* DRIFTS for investigation into the catalytic degradation of CB over (a) CeO_2, (b) $Ce_{0.7}Zr_{0.3}O_2$, and (c) S–$Ce_{0.7}Zr_{0.3}O_2$.

and redox properties of $Ce_{0.7}Zr_{0.3}O_2$ and S–$Ce_{0.7}Zr_{0.3}O_2$ are almost unaffected by Cl ions. NH_3-DRIFTS (Fig. S5†) was used to identify the type of acid sites on the used sample surface, and the values of A_B/A_L obtained from the spectra are listed in Table S2.† A significantly smaller A_B/A_L values of the used samples were observed compared with the fresh samples, indicating an increased proportion of Lewis acid sites on the sample surface after a reaction cycle. This is certainly consistent with previous analysis that the increased Lewis acid sites are attributable to oxygen vacancies.

3.3 Reaction pathway of CB degradation

Obviously, it can be concluded that both Zr doping and sulfur modification can significantly enhance the activity of CB degradation over a catalyst. To explore the essential effects of Lewis and Brønsted acid sites on catalytic activity and understand the inner reaction mechanism, *in situ* DRIFTS spectra for CB oxidation over CeO_2, $Ce_{0.7}Zr_{0.3}O_2$, and S–$Ce_{0.7}Zr_{0.3}O_2$ samples were collected at various temperatures (200–420 °C). As shown in Fig. 11, there are two negative peaks at 3717–3645 cm^{-1} and 3600–3100 cm^{-1} of all three samples, which are ascribed to the surface hydroxyl group interacting with CB.[28,50] Depending on the strength of these two bonds, it can be determined that the surface hydroxyl density of the three samples follows the sequence S–$Ce_{0.7}Zr_{0.3}O_2$ > $Ce_{0.7}Zr_{0.3}O_2$ > CeO_2, which is consistent with the order of acidity and catalytic performance. It is clear that abundant surface hydroxyl groups are favorable to the adsorption and activation of CB. The weak band at 2969 cm^{-1} is assigned to antisymmetric stretching of CH_3,[19] and the bonds centered at 1365 and 986 cm^{-1} are attributed to the ═C–O–C of surface phenol species and CH_2 of vinyl chloride.[7,53] It is worth noting that the band of vinyl chloride over S–$Ce_{0.7}Zr_{0.3}O_2$ is extremely weak. Moreover, an interesting phenomenon needs to be mentioned that some bands only appeared on the CeO_2 and $Ce_{0.7}Zr_{0.3}O_2$ samples, including the bands at 2929, 2849, 1474–1409, and 1224–1122 cm^{-1}. Among them, the first two bands corresponding to C═C and –CH– bonds are related to the formation of the enolic form, while the last two bonds reflect the production of chlorinated by-products. The band at 1474–1409 cm^{-1} is assigned to the C–Cl band of vinyl chloride.[53] According to a previous report, vinyl chloride is readily converted into a reactive carbonium ion by protons from hydroxyl groups of the acidic surface and then further transformed into chlorinated ethoxy species under the attack of nucleophilic oxygen species.[53] The presence of chlorinated ethoxy species is reflected by the band at 1224–1122 cm^{-1}. In fact, the chlorinated ethoxy species can readily divide into acetaldehyde and leave a Cl ion on the surface, causing the Cl-poisoning of catalysts. Moreover, the bonds resulting from the adsorption of acetic acid carboxylate species are observed at 1532 cm^{-1}.

Additionally, the adsorption bands of several important reaction intermediates, such as pyrocatechol (1622 cm^{-1}), cyclohexanone (1606 cm^{-1}), and acetate species or chlorinated acetate-type species (1569 cm^{-1}), were observed in the region of 1678–1554 cm^{-1}.[52,53] The accumulation of key intermediates is different, indicating multiple degradation pathways, which is related to the redox and acidity properties of the catalysts. Cyclohexanone, the most common intermediate, detected in the spectra of all three samples, is derived from the electrophilic attack of chlorobenzene by surface high-valence Lewis acid sites (Ce^{4+}, Zr^{4+}, and oxygen vacancy), and acetate species were considered to be a product of cyclohexanone oxidation through a ring-opening reaction. The pyrocatechol species were attributed to the oxidation and hydrolysis of CB by the surface hydroxyl group (Brønsted acid) and were detected only on the surface of the S–$Ce_{0.7}Zr_{0.3}O_2$ sample. Therefore, the following conclusions can be proposed that the degradation of CB over CeO_2 and $Ce_{0.7}Zr_{0.3}O_2$ occurs *via* the CB–cyclohexanone–maleic anhydride or maleic acid–acetate–CO_2 or small molecule hydrocarbon route, which is a typical oxidation pathway. For the CeO_2 sample, the oxidation of acetate is the rate-determining step for the reaction due to its fewer Lewis acid sites and lower oxygen reactivity as determined by the characterization techniques (XPS, O_2-TPD, H_2-TPR, pyridine-DRIFTS *etc.*). With the introduction of Zr ions, a large number of Lewis acid sites (Zr^{4+} and oxygen vacancies) appeared on the surface of the $Ce_{0.7}Zr_{0.3}O_2$ material, which greatly promoted the formation of cyclohexanone. It is not negligible that the Cl–M band is often produced during the oxidation of CB to cyclohexanone. The presence of Cl–M and Cl_2 generated through the Deacon reaction will lead to the formation of many toxic chlorine-containing by-products with high environmental risk, which has been verified by numerous bands of chlorinated organics in DRIFTS spectra. From the perspective of environmental safety, materials with rich Lewis acid sites are not desirable CB catalysts.

According to the literature, the degradation of CB on Brønsted acid-rich materials is dominated by a hydrolysis pathway with distinct features of abundant phenolic intermediate.[6] Therefore, the hydrolytic degradation pathway of CB on the S–$Ce_{0.7}Zr_{0.3}O_2$ sample was identified by the strongest bond corresponding to phenolic species on the DRIFTS spectra. The process of anchoring and hydrolysis of CB on the catalyst surface by interaction with surface hydroxyl groups is the source of the reaction, with the removal of Cl in the form of HCl and the production of phenol. Then, phenol was further hydrolyzed and oxidized to pyrocatechol, cyclohexanone and maleic acid and finally decomposed to CO_2 and H_2O. It is pretty obvious that Cl-deposition and Cl_2 formation are virtually non-occurring during this hydrolytic degradation process, and therefore very little chlorinated organics are produced. To sum up the above discussion, because of the synergistic effect of Lewis and Brønsted acid sites, the as-synthesized sample of S–$Ce_{0.7}Zr_{0.3}O_2$ can effectively eliminate CB with low toxic by-products and shows excellent stability.

4. Conclusion

In this work, Lewis and Brønsted acid sites were successfully introduced into the skeleton surface of 3DOM CeO_2 through zirconium doping and sulfur modification, respectively. The specific roles of different acid sites in CB degradation have been systematically studied. According to the activity data and characterizations, we found two different degradation modes, namely oxidation pathway and hydrolysis pathway. Among them, the former mainly occurs on the redox active site of materials and begins with the process of oxidation dechlorination accompanied by the formation of the M–Cl bond. With the accumulation of M–Cl bonds, the catalytic activity of CeO_2 to CB decreased rapidly. The introduction of Lewis acid can promote the activation of lattice oxygen and enhance the low temperature reducibility of the catalyst, which leads to the improvement of the catalytic oxidation performance. For $Ce_{0.7}Zr_{0.3}O_2$, the abundant Lewis acid sites on the surface accelerate the Deacon reaction and promote the desorption of ICs adsorbed on metal ions in the form of highly reactive Cl_2. The introduction of Lewis acid can effectively improve the activity and anti-toxicity of the catalyst, but will lead to the generation of more chlorine-containing by-products. The other pathway starts with the hydrolysis of chlorobenzene on Brønsted acid sites, with the removal of Cl poisoning species in the form of HCl, which is an efficient CB degradation pathway. The Brønsted acid sites on the surface of the catalyst can not only improve the degradation of CB, but also inhibit the production of chlorine-containing by-products and Cl_2 with high environmental risk. After a reaction cycle, the oxygen vacancies on the surface of the samples increased, which is conducive to the activation of lattice oxygen and the enhancement of surface acidity. HCl in the reaction stream can promote the desorption of sulfur species weakly adsorbed on the surface, but even after 106 h of reaction, the sulfur species strongly adsorbed on the $Ce_{0.7}Zr_{0.3}O_2$ with the main activity can be retained. Compared with other samples, because of the synergistic effect of Lewis and Brønsted acid sites, S–$Ce_{0.7}Zr_{0.3}O_2$ showed better CB degradation activity, stability, chlorine tolerance, water resistance, lower Cl_2 selectivity, and chlorine-containing by-product selectivity. This work can provide a reliable strategy for the design and development of environmentally friendly CVOC combustion catalysts by tuning the surface acidity to inhibit Cl poisoning and the formation of chlorinated pollutants.

Author contributions

Xuelong Lv: conceptualization; data curation; formal analysis; investigation; methodology; resources; writing – original draft. Songcai Cai: methodology; writing – review and editing. Jin Chen: methodology; resources. Dongxu Yan: methodology. Mingzhu Jiang: methodology. Jing Chen: writing – review and editing. Hongpeng Jia: conceptualization; supervision, writing – review and editing, project administration, funding acquisition.

Conflicts of interest

The authors declare no competing financial interest.

Acknowledgements

This work was supported by the National Key R&D Program of China [No. 2019YFC1806102]; the National Nature Science Foundation of China [No. 21976172]; the Science and Technology Planning Project of Fujian Province [2020Y01010042]; the FJIRSM&IUE Joint Research Fund [No. RHZX-2018-002]; and the "Key Research Program of Frontier Sciences" from the Chinese Academy of Sciences [No. QYZDB-SSW-DQC022].

References

1 B. Huang, C. Lei, C. Wei and G. Zeng, *Environ. Int.*, 2014, **71**, 118–138.
2 Z. Ren, Y. Lu, Q. Li, Y. Sun, C. Wu and Q. Ding, *Chemosphere*, 2018, **205**, 267–274.
3 J. Liu, X. Dai, Z. Wu and X. Weng, *Chin. Chem. Lett.*, 2020, **31**, 1410–1414.
4 Y. Wang, G. Wang, W. Deng, J. Han, L. Qin, B. Zhao, L. Guo and F. Xing, *Chem. Eng. J.*, 2020, **395**, 125172.
5 Y. Gu, S. Shao, W. Sun, H. Xia, X. Gao, Q. Dai, W. Zhan and X. Wang, *J. Catal.*, 2019, **380**, 375–386.
6 Q. Dai, J. Wu, W. Deng, J. Hu, Q. Wu, L. Guo, W. Sun, W. Zhan and X. Wang, *Appl. Catal., B*, 2019, **249**, 9–18.
7 W. Wang, Q. Zhu, Q. Dai and X. Wang, *Chem. Eng. J.*, 2017, **307**, 1037–1046.
8 J. Zhao, W. Xi, C. Tu, Q. Dai and X. Wang, *Appl. Catal., B*, 2020, **263**, 118237.
9 X. Zhang, L. Dai, Y. Liu, J. Deng, L. Jing, X. Yu, Z. Han, K. Zhang and H. Dai, *Catal. Sci. Technol.*, 2020, **10**, 3755–3770.
10 Q. Ying, Y. Liu, N. Wang, Y. Zhang and Z. Wu, *Appl. Surf. Sci.*, 2020, **515**, 145971.
11 X. Wang, W. Jiang, R. Yin, P. Sun, Y. Lu, Z. Wu and X. Weng, *J. Colloid Interface Sci.*, 2020, **574**, 251–259.
12 A. P. Amrute, C. Mondelli, M. Moser, G. Novell-Leruth, N. López, D. Rosenthal, R. Farra, M. E. Schuster, D. Teschner, T. Schmidt and J. Pérez-Ramírez, *J. Catal.*, 2012, **286**, 287–297.
13 M. Moser, C. Mondelli, T. Schmidt, F. Girgsdies, M. E. Schuster, R. Farra, L. Szentmiklósi, D. Teschner and J. Pérez-Ramírez, *Appl. Catal., B*, 2013, **132–133**, 123–131.
14 Z. Shi, P. Yang, F. Tao and R. Zhou, *Chem. Eng. J.*, 2016, **295**, 99–108.
15 H. Li, G. Lu, Q. Dai, Y. Wang, Y. Guo and Y. Guo, *Appl. Catal., B*, 2011, **102**, 475–483.
16 Y. Lao, N. Zhu, X. Jiang, J. Zhao, Q. Dai and X. Wang, *Catal. Sci. Technol.*, 2018, **8**, 4797–4811.
17 Y. Gu, X. Jiang, W. Sun, S. Bai, Q. Dai and X. Wang, *ACS Omega*, 2018, **3**, 8460–8470.

18 W. Deng, Q. Tang, S. Huang, L. Zhang, Z. Jia and L. Guo, *Appl. Catal., B*, 2020, **278**, 119336.
19 X. Fei, S. Cao, W. Ouyang, Y. Wen, H. Wang and Z. Wu, *Chem. Eng. J.*, 2020, **387**, 123411.
20 N. Li, J. Cheng, X. Xing, Y. Sun and Z. Hao, *J. Hazard. Mater.*, 2020, **393**, 122412.
21 Q. Dai, Z. Zhang, J. Yan, J. Wu, G. Johnson, W. Sun, X. Wang, S. Zhang and W. Zhan, *Environ. Sci. Technol.*, 2018, **52**, 13430–13437.
22 X. Dai, X. Wang, Y. Long, S. Pattisson, Y. Lu, D. J. Morgan, S. H. Taylor, J. H. Carter, G. J. Hutchings, Z. Wu and X. Weng, *Environ. Sci. Technol.*, 2019, **53**, 12697–12705.
23 X. Weng, P. Sun, Y. Long, Q. Meng and Z. Wu, *Environ. Sci. Technol.*, 2017, **51**, 8057–8066.
24 X. Feng, M. Tian, C. He, L. Li, J.-W. Shi, Y. Yu and J. Cheng, *Appl. Catal., B*, 2020, **264**, 118493.
25 Z. Zhang, J. Huang, H. Xia, Q. Dai, Y. Gu, Y. Lao and X. Wang, *J. Catal.*, 2018, **360**, 277–289.
26 Y. Wei, J. Liu, Z. Zhao, Y. Chen, C. Xu, A. Duan, G. Jiang and H. He, *Angew. Chem., Int. Ed.*, 2011, **50**, 2326–2329.
27 J. R. González-Velasco, A. Aranzabal, R. López-Fonseca, R. Ferret and J. A. González-Marcos, *Appl. Catal., B*, 2000, **24**, 33–43.
28 J. Chen, W. Xu, M. Jiang, J. Chen and H. Jia, *Appl. Catal., B*, 2020, **278**, 119263.
29 X. Weng, Q. Meng, J. Liu, W. Jiang, S. Pattisson and Z. Wu, *Environ. Sci. Technol.*, 2019, **53**, 884–893.
30 M. Moser, A. P. Amrute and J. Pérez-Ramírez, *Appl. Catal., B*, 2015, **162**, 602–609.
31 Y. Wang, H. Arandiyan, J. Scott, M. Akia, H. Dai, J. Deng, K.-F. Aguey-Zinsou and R. Amal, *ACS Catal.*, 2016, **6**, 6935–6947.
32 D. Li, K. Li, R. Xu, X. Zhu, Y. Wei, D. Tian, X. Cheng and H. Wang, *ACS Appl. Mater. Interfaces*, 2019, **11**, 19227–19241.
33 L. Xu, X. Wen, M. Chen, C. Lv, Y. Cui, X. Wu, C.-E. Wu, B. Yang, Z. Miao and X. Hu, *Fuel*, 2020, **282**, 125172.
34 X. Zhao, D. Xu, Y. Wang, Z. Zheng, K. Li, Y. Zhang, R. Zhan and H. Lin, *J. Hazard. Mater.*, 2020, 124349.
35 Y. Hu, B. Guo, Y. Fu, Y. Ren, G. Tang, X. Chen, B. Yue and H. He, *Chem. Commun.*, 2015, **51**, 14219–14222.
36 X. Liu, K. Wang, Y. Zhou, X. Tang, X. Zhu, R. Zhang, X. Zhang, X. Jiang and B. Liu, *Appl. Surf. Sci.*, 2019, **483**, 721–729.
37 X. Zhang, Y. Liu, J. Deng, X. Zhao, K. Zhang, J. Yang, Z. Han, X. Jiang and H. Dai, *Catal. Today*, 2020, **339**, 200–209.
38 A. S. Khder, E. A. El-Sharkawy, S. A. El-Hakam and A. I. Ahmed, *Catal. Commun.*, 2008, **9**, 769–777.
39 X. Li, X. Niu, P. Liu, X. Xu, D. Du and Y. Lin, *Sens. Actuators, B*, 2020, **321**, 128546.
40 M. Wahlqvist and A. Shchukarev, *J. Electron Spectrosc. Relat. Phenom.*, 2007, **156–158**, 310–314.
41 C. Dong, Z. Qu, Y. Qin, Q. Fu, H. Sun and X. Duan, *ACS Catal.*, 2019, **9**, 6698–6710.
42 Y. Shan, N. Gao, Y. Chen and S. Shen, *Ind. Eng. Chem. Res.*, 2019, **58**, 16370–16378.
43 C. Dong, Z. Qu, X. Jiang and Y. Ren, *J. Hazard. Mater.*, 2020, **391**, 122181.
44 B. Chen, B. Wu, L. Yu, M. Crocker and C. Shi, *ACS Catal.*, 2020, **10**, 6176–6187.
45 B. H. Aristizábal, C. Maya and C. M. D. Correa, *Appl. Catal., A*, 2008, **335**, 211–219.
46 J. Du, Z. Qu, C. Dong, L. Song, Y. Qin and N. Huang, *Appl. Surf. Sci.*, 2018, **433**, 1025–1035.
47 W. Wang, Q. Zhu, F. Qin, Q. Dai and X. Wang, *Chem. Eng. J.*, 2018, **333**, 226–239.
48 Z. Zhang, H. Xia, Q. Dai and X. Wang, *Appl. Catal., A*, 2018, **557**, 108–118.
49 L. Gu, X. Chen, Y. Zhou, Q. Zhu, H. Huang and H. Lu, *Chin. J. Catal.*, 2017, **38**, 607–615.
50 J. Zhao, C. Tu, W. Sun, H. Xia, H. Zhang, Q. Dai and X. Wang, *Catal. Sci. Technol.*, 2020, **10**, 742–756.
51 C. Contescu, V. Popa, J. Miller, E. Ko and J. Schwarz, *Chem. Eng. J.*, 1996, **10**, 265–272.
52 P. Sun, S. Zhai, J. Chen, J. Yuan, Z. Wu and X. Weng, *Appl. Catal., B*, 2020, **272**, 119015.
53 S. Bai, Q. Dai, X. Chu and X. Wang, *RSC Adv.*, 2016, **6**, 52564–52574.